

The transiting system HD 15337: a pair of nearly equal-mass sub-Neptunes on opposite sides of the radius gap

DAVIDE GANDOLFI,¹ LUCA FOSSATI,² JOHN H. LIVINGSTON,³ KEIVAN G. STASSUN,^{4,5} SASCHA GRZIWA,⁶
OSCAR BARRAGÁN,⁷ MALCOLM FRIDLUND,^{8,9} DARIA KUBYSHKINA,¹⁰ CARINA M. PERSSON,⁸ FEI DAI,^{11,12}
KRISTINE W. F. LAM,¹³ SIMON ALBRECHT,¹⁴ PAUL BECK,¹⁵ ANDERS BO JUSTESEN,¹⁴ JUAN CABRERA,¹⁶
WILLIAM D. COCHRAN,¹⁷ SZILARD CSIZMADIA,¹⁶ JEROME P. DE LEON,³ HANS J. DEEG,^{15,18} PHILIPP EIGMÜLLER,¹⁶
MICHAEL ENDL,¹⁷ ANDERS ERIKSON,¹⁶ MASSIMILIANO ESPOSITO,¹⁹ AKIHIKO FUKUI,^{15,20,21} EIKE W. GUENTHER,¹⁹
ARTIE P. HATZES,¹⁹ DIEGO HIDALGO,¹⁵ TERUYUKI HIRANO,²² MARIA HJORTH,¹⁴ PETR KABATH,²³ EMIL KNUDSTRUP,¹⁴
JUDITH KORTH,²⁴ MIKKEL N. LUND,¹⁴ RAFAEL LUQUE,¹⁵ SAVITA MATHUR,¹⁵ PILAR MONTAÑES RODRÍGUEZ,¹⁵
NORIO NARITA,^{3,15,25,26} DAVID NESPRAL,^{15,18} PRAJWAL NIRLAULA,²⁷ GRZEGORZ NOWAK,^{15,18} ENRIC PALLE,^{15,18}
MARTIN PÄTZOLD,²⁴ JORGE PRIETO-ARRANZ,^{15,18} HEIKE RAUER,^{13,16,28} SETH REDFIELD,²⁹ IGNASI RIBAS,^{30,31}
MAREK SKARKA,^{32,33} ALEXIS M. S. SMITH,¹⁶ VINCENT VAN EYLEN,¹² AND THE *TESS* TEAM

¹*Dipartimento di Fisica, Università degli Studi di Torino, via Pietro Giuria 1, I-10125, Torino, Italy*

²*Space Research Institute, Austrian Academy of Sciences, Schmiedlstrasse 6, A-8041 Graz, Austria*

³*Department of Astronomy, University of Tokyo, 7-3-1 Hongo, Bunkyo-ku, Tokyo 113-0033, Japan*

⁴*Vanderbilt University, Department of Physics & Astronomy, 6301 Stevenson Center Ln., Nashville, TN 37235, US*

⁵*Fisk University, Department of Physics, 1000 17th Ave. N., Nashville, TN 37208, US*

⁶*Rheinisches Institut für Umweltforschung, Abteilung Planetenforschung an der Universität zu Köln, Aachener Strasse 209, 50931 Köln, Germany*

⁷*Oxford Astrophysics, Department of Physics, University of Oxford, Denys Wilkinson Building, Keble Road, Oxford, OX1 3RH, UK*

⁸*Department of Space, Earth and Environment, Chalmers University of Technology, Onsala Space Observatory, 439 92 Onsala, Sweden*

⁹*Leiden Observatory, University of Leiden, PO Box 9513, 2300 RA, Leiden, The Netherlands*

¹⁰*Space Research Institute, Austrian Academy of Sciences, Schmiedlstrasse 6, A-8041 Graz, Austria*

¹¹*Department of Physics and Kavli Institute for Astrophysics and Space Research, Massachusetts Institute of Technology, Cambridge, MA, 02139, USA*

¹²*Department of Astrophysical Sciences, Princeton University, 4 Ivy Lane, Princeton, NJ, 08544, USA*

¹³*Center for Astronomy and Astrophysics, TU Berlin, Hardenbergstr. 36, 10623 Berlin, Germany*

¹⁴*Stellar Astrophysics Centre, Department of Physics and Astronomy, Aarhus University, Ny Munkegade 120, DK-8000 Aarhus C, Denmark*

¹⁵*Instituto de Astrofísica de Canarias, C/Vía Láctea s/n, 38205 La Laguna, Spain*

¹⁶*Institute of Planetary Research, German Aerospace Center, Rutherfordstrasse 2, 12489 Berlin, Germany*

¹⁷*Department of Astronomy and McDonald Observatory, University of Texas at Austin, 2515 Speedway, Stop C1400, Austin, TX 78712, USA*

¹⁸*Departamento de Astrofísica, Universidad de La Laguna, 38206 La Laguna, Spain*

¹⁹*Thüringer Landessternwarte Tautenburg, Sternwarte 5, D-07778 Tautenburg, Germany*

²⁰*Department of Earth and Planetary Science, University of Tokyo, 7-3-1 Hongo, Bunkyo-ku, Tokyo 113-0033, Japan*

²¹*Subaru Telescope Okayama Branch Office, National Astronomical Observatory of Japan, NINS, 3037-5 Honjo, Kamogata, Asakuchi, Okayama 719-0232, Japan*

²²*Department of Earth and Planetary Sciences, Tokyo Institute of Technology, 2-12-1 Ookayama, Meguro-ku, Tokyo 152-8551, Japan*

²³*Astronomical Institute AS CR, Fricova 298, 25165, Ondřejov, Czech Republic*

²⁴*Rheinisches Institut für Umweltforschung an der Universität zu Köln, Aachener Strasse 209, 50931 Köln, Germany*

²⁵*Astrobiology Center, NINS, 2-21-1 Osawa, Mitaka, Tokyo 181-8588, Japan*

²⁶*National Astronomical Observatory of Japan, NINS, 2-21-1 Osawa, Mitaka, Tokyo 181-8588, Japan*

²⁷*Department of Earth, Atmospheric and Planetary Sciences, Massachusetts Institute of Technology, Cambridge, MA 02139*

²⁸*Institute of Geological Sciences, FU Berlin, Malteserstr. 74-100, D-12249 Berlin*

²⁹*Astronomy Department and Van Vleck Observatory, Wesleyan University, Middletown, CT 06459, USA*

³⁰*Institut de Ciències de l'Espai (ICE, CSIC), Campus UAB, C/ de Can Magrans s/n, E-08193 Bellaterra, Spain*

³¹*Institut d'Estudis Espacials de Catalunya (IEEC), C/ Gran Capità 2-4, E-08034 Barcelona, Spain*

³²*Astronomical Institute AS CR, Fricova 298, 25165, Ondřejov, Czech Republic*

³³*Department of Theoretical Physics and Astrophysics, Masaryk University, Kotlářská 2, 61137 Brno, Czech Republic*

ABSTRACT

We report the discovery of two small planets transiting the star HD 15337 (TOI-402, TIC 120896927), a bright ($V=9$) K1 V dwarf observed by the Transiting Exoplanet Survey Satellite (*TESS*) in Sectors 3 and 4. We combine the *TESS* photometry with archival HARPS spectra to confirm the planetary nature of the transit signals and derive the masses of the two transiting planets. With an orbital period of 4.8 days, a mass of $7.63 \pm 0.94 M_{\oplus}$ and a radius of $1.585 \pm 0.056 R_{\oplus}$, HD 15337 b joins the growing group of short-period planets known to have a rocky terrestrial composition. HD 15337 c has an orbital period of 17.2 days, a mass of $7.37^{+1.63}_{-1.61} M_{\oplus}$ and a radius of $2.309^{+0.110}_{-0.103} R_{\oplus}$, suggesting that the planet might be surrounded by a thick atmospheric envelope. The two planets have virtually the same masses and lie on opposite sides of the radius gap, and are thus an excellent testbed for planet formation and evolution theories. Assuming that HD 15337 c hosts a hydrogen-dominated envelope, we employed a recently developed planet atmospheric evolution algorithm in a Bayesian framework to estimate the history of the high-energy emission of the host star concluding that at 150 Myr it ranged between 1.5 and 93 times that of the current Sun.

Keywords: Planetary systems – Planets and satellites: individual: HD 15337 b – Stars: fundamental parameters – Stars: individual: HD 15337 – Techniques: photometric – Techniques: radial velocities

1. INTRODUCTION

Successfully launched in April 2018, NASA’s Transiting Exoplanet Survey Satellite (*TESS*) is providing a significant step in understanding the diversity of exoplanets. *TESS* is performing an all-sky photometric search for planets transiting bright stars ($6 < V < 11$), so that detailed characterizations of the planets and their atmospheres can be performed (Ricker et al. 2015). The survey is broken up into 26 sectors – each sector being observed for ~ 28 days and consisting of 4 cameras with a combined field-of-view of $24^{\circ} \times 96^{\circ}$. Candidate alerts and full-frame images are released every month. As of March 2019, *TESS* has already announced the discovery of about a dozen transiting planets (see, e.g., Esposito et al. 2018; Gandolfi et al. 2018; Huang et al. 2018; Jones et al. 2018; Nielsen et al. 2018; Quinn et al. 2019; Trifonov et al. 2019).

TESS has already led to the detection of promising systems in terms of planet atmospheric characterization, such as π Men, which is a bright ($V=5.65$) star hosting a transiting super-Earth with a bulk density consistent with either a primary, hydrogen-dominated atmosphere, or a secondary, probably $\text{CO}_2/\text{H}_2\text{O}$ -dominated, atmosphere (Gandolfi et al. 2018; Huang et al. 2018). The discovery of such systems is central for performing multi-wavelength transmission spectroscopy observations to identify the nature of the atmosphere, thus constraining planetary atmospheric evolution models.

TESS enables also the discovery of multi-planet systems for which both mass and radius can be precisely measured. Since such planets orbit the same star, differences in average density and atmospheric structure among planets belonging to the same system can be as-

cribed mainly to differences in planetary mass and orbital separation (see, e.g., Guenther et al. 2017; Prieto-Arranz et al. 2018). This greatly simplifies modeling of their past evolution history, thus constraining how these planets formed (Alibert et al. 2005; Alibert & Benz 2017). In this respect, even more significant are multi-planet systems in which two or more planets have similar masses, as differences in radii would most likely be due to the different orbital separations.

In this paper we report the discovery of two small planets transiting the bright ($V=9$) star HD 15337 (Table 1), a K1 dwarf observed by *TESS* in Sectors 3 and 4. We combined the *TESS* photometry with archival HARPS radial velocities (RVs) to confirm the planetary nature of the transit signals and derive the masses of the two planets. The paper is organized as follows. In Sect. 2, we present the *TESS* photometry and the detection of the transit signals. In Sect. 3, we present the archival HARPS spectra. The properties of the host star are reported in Sect. 4. We present the frequency analysis of the HARPS RVs in Sect. 5 and the data modeling in Sect. 6. Results, discussions, and summary are given in Sect. 7.

2. *TESS* PHOTOMETRY

HD 15337 (TIC 120896927) was observed by *TESS* Camera #2 in Sectors 3 and 4 (CCDs #3 and #4, respectively) from 20 September 2018 to 15 November 2018, and will not be observed further during the nominal two-year *TESS* mission. Photometry was interrupted when the satellite was re-pointed for data downlink, from $\text{BJD}_{\text{TDB}} = 2458395.4$ to $\text{BJD}_{\text{TDB}} = 2458396.6$ in Sector 3, and from $\text{BJD}_{\text{TDB}} = 2458423.5$

Table 1. Main identifiers, coordinates, proper motion, parallax, and optical and infrared magnitudes of HD 15337.

Parameter	Value	Source
<i>Main identifiers</i>		
HD	15337	
HIP	11433	Hipparcos
TIC	120896927	TIC ^a
TOI	402	<i>TESS</i> Alerts
<i>Gaia</i> DR2	5068777809824976256	<i>Gaia</i> DR2 ^b
<i>Equatorial coordinates</i>		
RA (J2000.0)	02 ^h 27 ^m 28.3781 ^s	<i>Gaia</i> DR2 ^b
DEC (J2000.0)	−27° 38′ 06.7417″	<i>Gaia</i> DR2 ^b
<i>Proper motion and parallax</i>		
$\mu_{\alpha} \cos \delta$ (mas yr ^{−1})	−73.590 ± 0.057	<i>Gaia</i> DR2 ^b
μ_{δ} (mas yr ^{−1})	−211.614 ± 0.082	<i>Gaia</i> DR2 ^b
Parallax (mas)	17.01 ± 0.81	<i>Gaia</i> DR2 ^b
<i>Magnitudes</i>		
B_T	10.170 ± 0.027	<i>Tycho</i> -2 ^c
V_T	9.184 ± 0.018	<i>Tycho</i> -2 ^c
G	8.8560 ± 0.0002	<i>Gaia</i> DR2 ^b
G_{BP}	9.3194 ± 0.0011	<i>Gaia</i> DR2 ^b
G_{RP}	8.2708 ± 0.0016	<i>Gaia</i> DR2 ^b
J	7.553 ± 0.019	2MASS ^d
H	7.215 ± 0.034	2MASS ^d
K_s	7.044 ± 0.018	2MASS ^d
$W1(3.35 \mu\text{m})$	6.918 ± 0.054	ALLWISE ^e
$W2(4.6 \mu\text{m})$	7.048 ± 0.020	ALLWISE ^e
$W3(11.6 \mu\text{m})$	7.015 ± 0.017	ALLWISE ^e
$W4(22.1 \mu\text{m})$	6.916 ± 0.072	ALLWISE ^e

NOTE—(a) *TESS* Input Catalog (Stassun et al. 2018b); (b) *Gaia* Data Release 2 (Gaia Collaboration et al. 2018); (c) *Tycho*-2 Catalog (Høg et al. 2000); (d) Two-micron All Sky Survey (Cutri et al. 2003); (e) Wide-field Infrared Survey Explorer catalog (Cutri & et al. 2013).

to $\text{BJD}_{\text{TDB}} = 2458424.6$ in Sector 4. There is an additional data gap in Sector 4 from $\text{BJD}_{\text{TDB}} = 2458418.5$ to $\text{BJD}_{\text{TDB}} = 2458421.2$, which was caused by an interruption in communications between the instrument and spacecraft.

TESS objects of interest (TOIs) are announced publicly via the MIT *TESS* data alerts web portal.¹ TOIs 402.01 and 402.02 were announced on 16 January 2019 and 31 January 2019, respectively, in association with the HD 15337 photometry. The *TESS* pixel data and

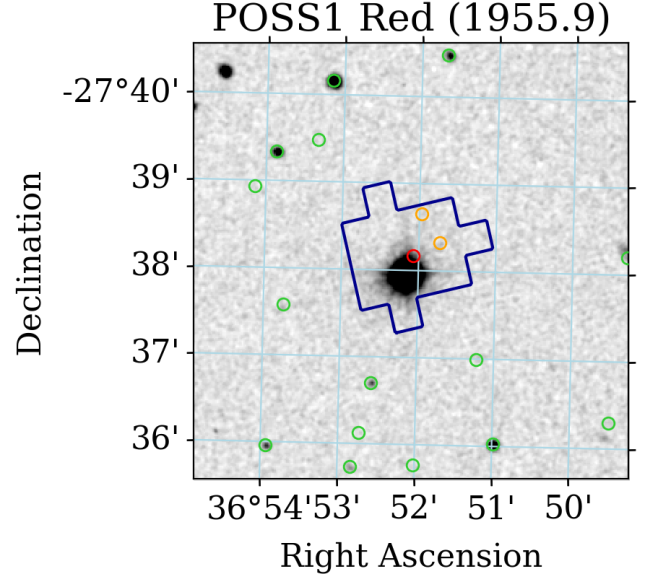


Figure 1. 5′ × 5′ 103aE emulsion image taken in 1955 from the POSS1-E survey, with the SPOC photometric aperture overplotted in blue (*TESS* pixel size is 21″), and the positions of *Gaia* DR2 sources (J2015.5) within 2′ of HD 15337 indicated by circles. HD 15337 is in red, nearby sources contributing more than 1% of their flux to the aperture are in orange (see Sect. 2), and other sources are in green. Due to the proper motion of HD 15337, there is a ∼14″ offset between its *Gaia* position and its position in the image.

light curves produced by the Science Processing Operations Center (SPOC; Jenkins et al. 2016) at NASA Ames Research Center were subsequently made publicly available via the Mikulski Archive for Space Telescopes (MAST).² We iteratively searched the SPOC light curves for transit signals using the Box-least-squares algorithm (BLS; Kovács et al. 2002), after fitting and removing stellar variability using a cubic spline with knots every 1.0 days. We recovered two signals corresponding to the TOIs, but no other significant signals were detected. We also tried removing variability using the wavelet-based filter routines VARLET and PHALET, but it did not change the BLS results; we are thus confident that the two signals are robustly detected and are not the result of data artefacts resulting from the choice of variability model or residual instrumental systematic signals. The phase-folded transit signals are shown in Fig. 6.

The SPOC light curves are produced using an optimized aperture, which is shown in Fig. 1. We produced light curves from the *TESS* pixel data using a series of apertures (Gandolfi et al. 2018; Esposito et al. 2018),

¹ <https://tess.mit.edu/alerts>.

² <https://mast.stsci.edu>.

and found that larger apertures than the SPOC aperture shown in Fig. 1 minimized the 6.5 hour combined differential photometric precision (CDPP) noise metric (Christiansen et al. 2012). However, the transit signals recovered from these light curves were slightly less significant, which we attribute to the improvement in light curve quality afforded by the Presearch Data Conditioning (PDC; Smith et al. 2012; Stumpe et al. 2012) pipeline used by the SPOC, which corrects for common-mode systematic noise; for this reason, we opted to analyze the SPOC light curves for the remainder of the analysis in this paper.

To investigate the possibility of diluting flux from stars other than HD 15337, we visually inspected archival imaging and compared *Gaia* DR2 (Gaia Collaboration et al. 2018) source positions with the SPOC photometric aperture. We used the coordinates of HD 15337 from the *TESS* Input Catalog³ (TIC; Stassun et al. 2018b) to retrieve *Gaia* DR2 sources using a search radius of 3'. In archival imaging taken in 1955 from the POSS-I survey⁴, HD 15337 is offset from its current position by $\sim 14''$ due to proper motion, but this is not sufficient to completely rule out chance alignment with a background source; however, such an alignment with a bright source is highly unlikely. Assuming the *TESS* point spread function (PSF) can be approximated by a 2D Gaussian profile with a FWHM of $\sim 25''$, we found that 98.5% of the flux from HD 15337 is within the SPOC aperture. Approximating the *TESS* bandpass with the *Gaia* G_{RP} bandpass, the transit signals from HD 15337 should be diluted by less than 0.01%; HD 15337 is the only star contributing flux to the aperture that is bright enough to be the source of the transit signals. Two other *Gaia* DR2 sources (5068777809825770112 and 5068777745400963584) are also within the SPOC aperture, but they are too faint to yield significant dilution ($G_{\text{RP}} \approx 19$ mag). Fig. 1 shows the archival image, along with *Gaia* DR2 source positions and the SPOC photometric aperture.

3. HARPS SPECTROSCOPIC OBSERVATIONS

HD 15337 was observed between 15 December 2003 and 06 September 2017 UT with the High Accuracy Radial velocity Planet Searcher (HARPS) spectrograph ($R \approx 115\,000$, Mayor et al. 2003) mounted at the ESO-3.6 m telescope, as part of the observing programs 072.C-0488, 183.C-0972, 192.C-0852, 196.C-1006, and 198.C-0836. We retrieved the publicly available reduced

spectra from the ESO archive, along with the cross-correlation function (CCF) and its bisector, computed from the dedicated HARPS pipeline using a K5 numerical mask (Baranne et al. 1996). On June 2015, the HARPS fiber bundle was upgraded and a new set of octagonal fibers, with improved mode-scrambling capabilities, were installed (Lo Curto et al. 2015). To account for the RV offset caused by the instrument refurbishment, we treated the HARPS RVs taken before/after June 2015 as two different data sets. Tables 3 and 4 list the HARPS RVs taken with the old and new fiber bundle, along with the RV uncertainties, the full width at half maximum (FWHM) and bisector span (BIS) of the CCF, the exposure times, and the signal-to-noise ratio (S/N) per pixel at 5500 Å. Time stamps are given in barycentric Julian Date in the barycentric dynamical time (BJD_{TDB}). We rejected two data points – marked with asterisks in Tables 3 and 4 – because of poor S/N ratio (BJD_{TDB} = 2455246.519846) or systematics (BJD_{TDB} = 2457641.794439).

4. STELLAR FUNDAMENTAL PARAMETERS

4.1. Spectroscopic parameters

We co-added the HARPS spectra obtained with the old and new fiber bundle separately to get two combined spectra with S/N per pixel at 5500 Å of 590 (old fiber) and 490 (new fiber). We derived the spectroscopic parameters of HD 15337 from the co-added HARPS spectra using Spectroscopy Made Easy (SME), a spectral analysis tool that calculates synthetic spectra and fits them to high-resolution observed spectra using a χ^2 minimizing procedure. The analysis was performed with the non-LTE SME version 5.2.2, along with ATLAS 12 one-dimensional model atmospheres (Kurucz 2013).

We estimated a micro-turbulent velocity of $v_{\text{mic}} = 0.80 \pm 0.10 \text{ km s}^{-1}$ from the empirical calibration equations for Sun-like stars from Bruntt et al. (2010). The effective temperature T_{eff} was measured fitting the wings of the H_{α} and H_{β} lines, as well as the Na I doublet at 5890 and 5896 Å (Fuhrmann et al. 1993; Axer et al. 1994; Fuhrmann et al. 1994, 1997b,a). The surface gravity $\log g_{\star}$ was determined from the wings of the Ca I $\lambda 6102$, $\lambda 6122$, $\lambda 6162$ Å triplet, and the Ca I $\lambda 6439$ Å line, as well as from the Mg I $\lambda 5167$, $\lambda 5173$, $\lambda 5184$ Å triplet. We measured the iron abundance [Fe/H], the macroturbulent velocity v_{mac} , and the projected rotational velocity $v \sin i_{\star}$ by simultaneously fitting the unblended iron lines in the spectral region 5880–6600 Å.

Our analyses applied to the two stacked HARPS spectra provide consistent results, well within the uncertainties. The final adopted values are listed in Table 2. We derived an effective temperature of $T_{\text{eff}} =$

³ Available at <https://mast.stsci.edu/portal/Mashup/Clients/Mast/Portal.html>.

⁴ Available at http://archive.stsci.edu/cgi-bin/dss_form.

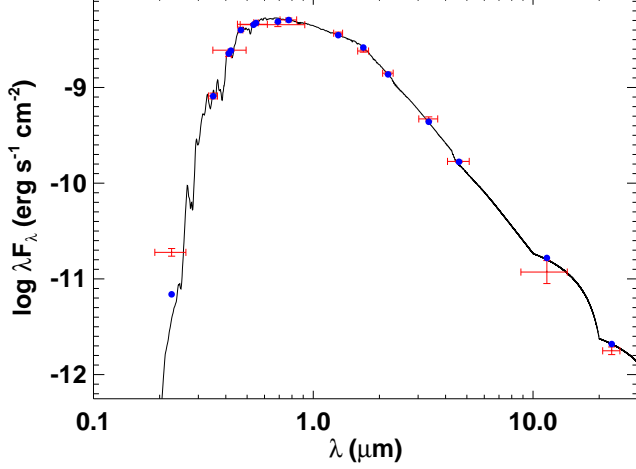


Figure 2. Spectral energy distribution (SED) of HD 15337. Red symbols represent the observed photometric measurements, where the horizontal bars represent the effective width of the passband. Blue symbols are the model fluxes from the best-fit Kurucz atmosphere model (black).

5125 ± 50 K, surface gravity $\log g_* = 4.40 \pm 0.10$ (cgs), and an iron abundance relative to solar of $[\text{Fe}/\text{H}] = 0.15 \pm 0.08$ dex. We also measured a calcium abundance of $[\text{Ca}/\text{H}] = 0.08 \pm 0.04$ dex and a sodium abundance of $[\text{Na}/\text{H}] = 0.27 \pm 0.054$ dex. We found a macro-turbulent velocity of $v_{\text{mac}} = 3.0 \pm 1.0$ km/s in agreement with the value predicted from the empirical equations of Doyle et al. (2014). The projected rotational velocity was found to be $v \sin i_* = 1.0 \pm 1.0$ km s $^{-1}$.

4.2. Stellar mass, radius, age and interstellar extinction

We performed an analysis of the broadband spectral energy distribution (SED) together with the *Gaia* Data Release 2 (DR2; Gaia Collaboration et al. 2018) parallax in order to determine an empirical measurement of the stellar radius, following the procedures described in Stassun & Torres (2016), Stassun et al. (2017), and Stassun et al. (2018a). We retrieved the B_T and V_T magnitudes from the *Tycho*-2, the Strömgren *ubvy* magnitudes from Paunzen (2015), the *BVgr* magnitudes from APASS, the *JHK_S* magnitudes from 2MASS (Cutri et al. 2003), the *W1–W4* magnitudes from *ALLWISE* (Cutri & et al. 2013), and the *G* magnitude from *Gaia* DR2 (Gaia Collaboration et al. 2018). Together, the available photometry spans the full stellar SED over the wavelength range 0.35–22 μm (Fig. 2). In addition, we pulled the NUV flux from *GALEX* in order to assess the level of chromospheric activity, if any.

We performed a fit using Kurucz stellar atmosphere models, with the fitted parameters being the effective

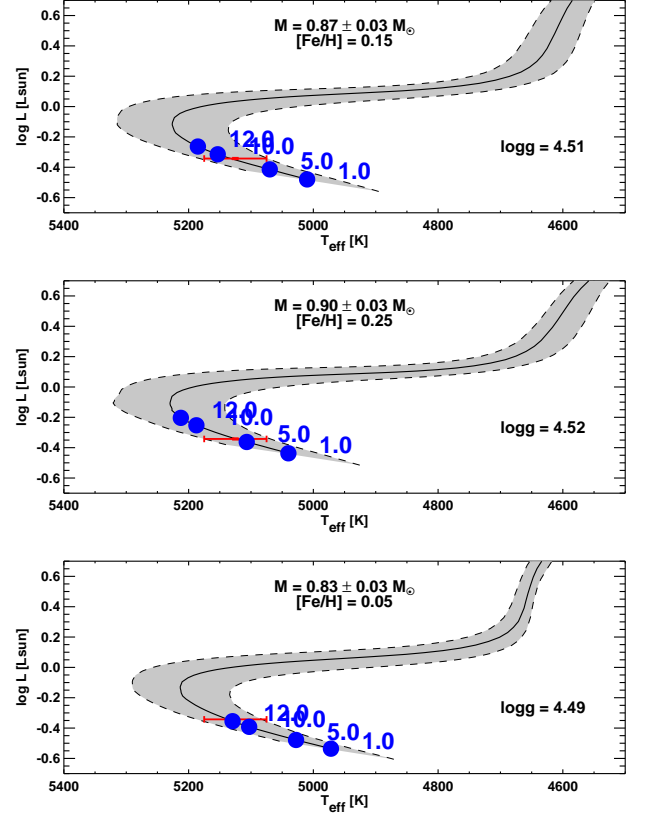


Figure 3. Hertzsprung-Russell Diagram for HD 15337 based on the observed effective temperature and bolometric luminosity, the latter computed directly from F_{bol} and the *Gaia* parallax-based distance. Each panel compares the observed properties of the star to evolutionary tracks from the Yonsei-Yale models (Yi et al. 2001; Spada et al. 2013) for different permitted combinations of stellar mass and metallicity. Blue points with labels represent the model ages in Gyr. The central panel represents that case most compatible with all of the available data, including the stellar age of ≈ 5.1 Gyr as determined from the observed chromospheric activity and stellar rotation period (see the text).

temperature T_{eff} and iron abundance $[\text{Fe}/\text{H}]$, as well as the interstellar extinction A_v , which we restricted to the maximum line-of-sight value from the dust maps of Schlegel et al. (1998). The broadband SED is largely insensitive to the surface gravity ($\log g_*$), thus we simply adopted the value from the initial spectroscopic analysis presented in the previous subsection. The resulting fit is excellent (Figure 2) with a reduced χ^2 of 2.3 (excluding the *GALEX* NUV flux, which is consistent with a modest level of chromospheric activity). The best fit parameters effective temperature and iron content are $T_{\text{eff}} = 5130 \pm 50$ K and $[\text{Fe}/\text{H}] = 0.1^{+0.2}_{-0.1}$ dex, respectively, in excellent agreement with the spectroscopic values (Sect. 4.1). We found that the reddening of HD 15337

is consistent with zero ($A_v = 0.02 \pm 0.02$ mag), as expected given the relatively short distance to the star (~ 45 pc). Integrating the unreddened model SED gives the bolometric flux at Earth of $F_{\text{bol}} = 7.29 \pm 0.08 \times 10^{-9}$ erg s cm $^{-2}$. Taking the F_{bol} and T_{eff} together with the *Gaia* DR2 parallax, adjusted by +0.08 mas to account for the systematic offset reported by *Stassun & Torres* (2018), gives the stellar radius as $R_\star = 0.856 \pm 0.017 R_\odot$. Finally, estimating the stellar mass from the empirical relations of *Torres et al.* (2010) and a 6% error from the empirical relation itself gives a stellar mass of $M_\star = 0.91 \pm 0.06 M_\odot$.

We can refine the stellar mass estimate by taking advantage of the observed chromospheric activity, which can constrain the age of the star via empirical relations. For example, taking the chromospheric activity indicator, $\log R'_{\text{HK}} = -4.916 \pm 0.038$ from *Gomes da Silva et al.* (2014) and applying the empirical relations of *Mamajek & Hillenbrand* (2008), gives a predicted age of 5.1 ± 0.8 Gyr. As shown in Fig. 3, according to the Yonsei-Yale stellar evolutionary models (*Yi et al.* 2001; *Spada et al.* 2013), this age is most compatible with a stellar mass of $M_\star = 0.90 \pm 0.03 M_\odot$ and $[\text{Fe}/\text{H}] = 0.25$, which with the empirically determined stellar radius implies a stellar $\log g_\star = 4.52 \pm 0.02$ (cgs), in good agreement with the spectroscopic value of $\log g_\star = 4.40 \pm 0.10$ (cgs).

Other combinations of stellar mass and metallicity are compatible with the observed effective temperature and radius (Fig. 3), however they require ages that are incompatible with that predicted by the chromospheric R'_{HK} emission. Finally, we can further corroborate the activity-based age estimate by also using empirical relations to predict the stellar rotation period from the activity. For example, the empirical relation between R'_{HK} and rotation period from *Mamajek & Hillenbrand* (2008) predicts a rotation period for this star of ≈ 42 days, which is compatible with the observed rotation period derived from the HARPS RVs and activity indicators ($P_{\text{rot}} = 36.5$ days; see the following section).

5. FREQUENCY ANALYSIS OF THE HARPS MEASUREMENTS

We performed a frequency analysis of the HARPS time-series to search for the Doppler reflex motion induced by the two transiting planets discovered by *TESS*. We accounted for the RV offset between the two different set-ups of the instrument (old and new fiber bundle) using the value of 19.6 m s^{-1} derived from the joint analysis presented in Sect. 6, which is in good agreement with the expected offset for a slowly rotating K1 V star, such as HD 15337 (*Lo Curto et al.* 2015).

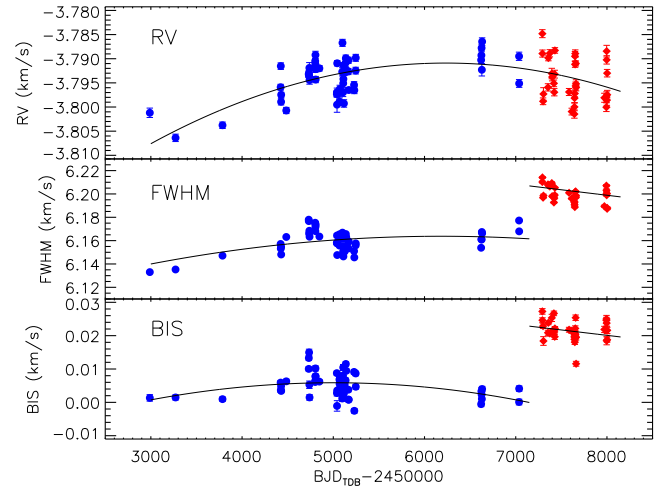


Figure 4. Offset-corrected HARPS RVs of HD 15337 (upper panel), and FWHM and BIS of the cross-correlation function (middle and lower panels). The blue circles and red diamonds mark the measurements acquired with the old and new fiber bundle, respectively. The thick lines mark the best-fitting parabolic curves to the data (see the text).

The offset-corrected HARPS RVs are displayed in Fig. 4 (upper panel), along with the FWHM and BIS time-series (middle and lower panel, respectively). The generalized Lomb-Scargle (GLS) periodogram (*Zechmeister & Kürster* 2009) of the combined RV data shows significant power at frequencies lower than the inverse of the temporal baseline of the HARPS observations. A similar trend is observed in the FWHM obtained with the old fiber bundle (middle panel, blue circles), suggesting that the RV trend might be due to long-term stellar variability (e.g., magnetic cycles)⁵. Alternatively, the RV trend might be induced by a long period orbiting companion, while the long-term variation of the FWHM might be ascribable to the steady instrument de-focusing observed between 2004 and 2015 (*Lo Curto et al.* 2015).

The upper panel of Fig. 5 shows the GLS periodogram of the combined HARPS RVs, following the subtraction of the best-fitting quadratic trend (cfr. Fig. 4). The peaks with the highest power are found at the orbital frequencies of the two transiting planets ($f_c = 0.058$ c/d and $f_b = 0.210$ c/d), with false-alarm probabilities⁶ (FAPs) of $\approx 1\%$ and RV semi-amplitude of about 2.0 – 2.5 m s^{-1} . The periodogram of the RV residuals after subtracting the signal of the outer planet (Fig. 5, sec-

⁵ We note that the FWHM and BIS offsets between the two instrument set-ups are unknown.

⁶ The false-alarm probability was derived using the bootstrap method described in (*Kuerster et al.* 1997).

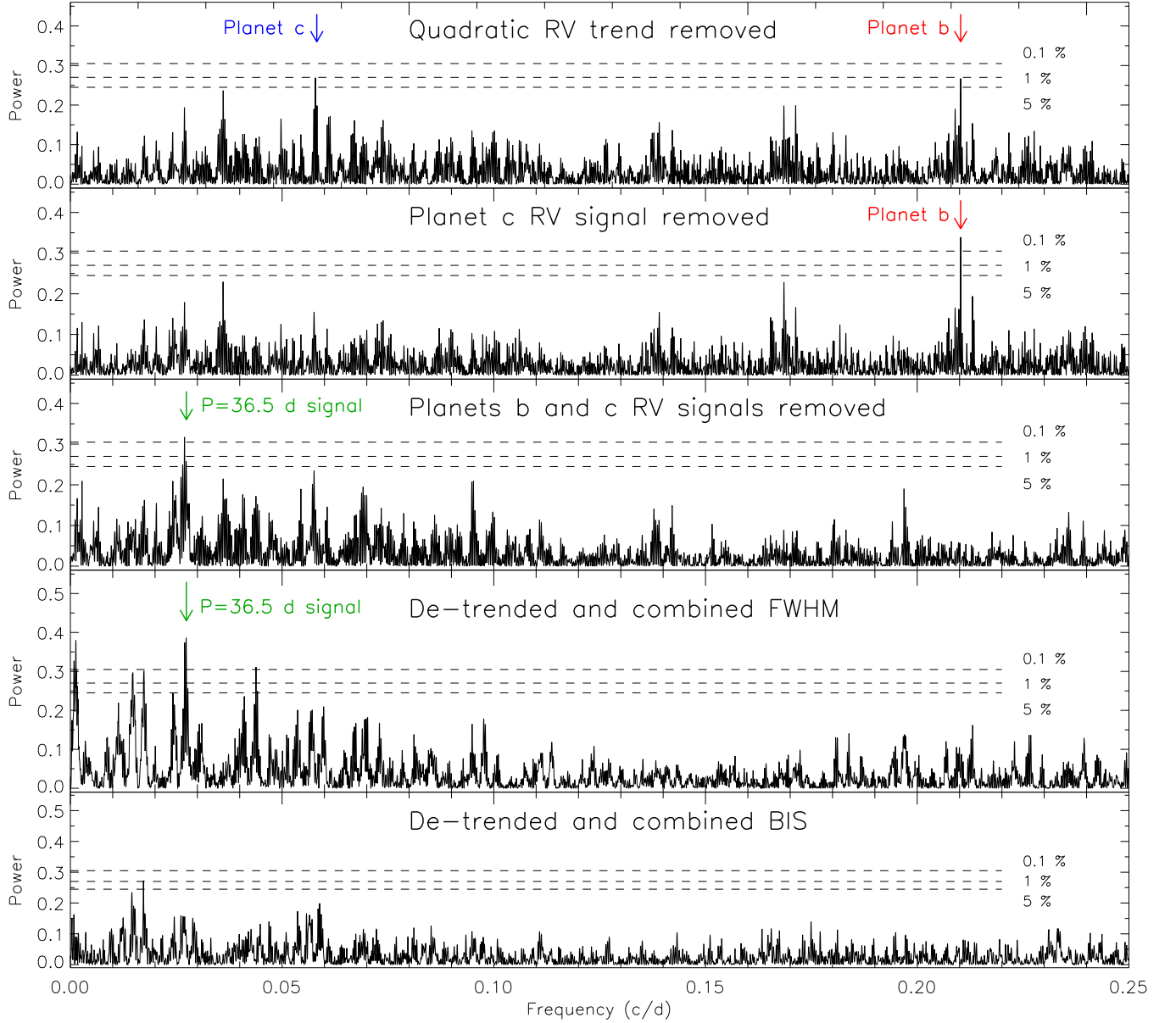


Figure 5. Generalized Lomb-Scargle periodograms of 1) the combined HARPS RV measurements, following the subtraction of the quadratic trend (first panel); 2) the RV residuals after subtracting the signal of HD 15337 c (second panel); 3) the RV residuals after subtracting the signal of HD 15337 b and c (third panel); the FWHM of the cross-correlation function (fourth panel); the bisector span (BIS) of the cross-correlation function (fifth panel). The dashed horizontal lines mark the false-alarm probability at 0.1, 1 and 5 %. The frequencies of the two transiting planets, as well as of the signal at 36.5 days are marked with vertical arrows.

ond panel), shows a significant peak (FAP < 0.1 %) at the frequency of the inner planet. The two peaks have no counterparts in the periodograms of the activity indicators⁷ (FWHM and BIS; Fig. 5, fourth and fifth panel), suggesting that the signals are induced by two orbiting

planets with periods of 4.8 and 17.2 days. Finally, the GLS periodogram of the RV residuals after subtracting the quadratic trend and the signals of the two planets (Fig. 5, third panel) displays a peak with a FAP < 0.1 % at ~36.5 days, which is also significantly detected in the periodogram of the FWHM (fourth panel). We interpreted the 36.5-day signal as the rotation period of the star. It agrees with the value expected from the R'_{HK}

⁷ We combined the activity indicators from the two HARPS fibers by subtracting the best fitting second order polynomials shown in Fig. 4.

activity indicator (Sect. 4.2) and from combining the stellar projected rotational velocity and stellar radius.

6. JOINT ANALYSIS

We performed a joint analysis of the *TESS* light curve (Sect. 2) and RV measurements (Sect. 3) using the software suite `pyaneti`, which allows for parameter estimation from posterior distributions calculated using Markov chain Monte Carlo methods.

We extracted ~ 8 hours of *TESS* data points centered around each of the transits observed by *TESS* during Sector 3 and 4. We de-trended the photometric segments with the code `exotrending` using a second-order polynomial fitted to the out-of-transit data. As described in Sect. 3, we rejected 2 HARPS RVs and used the remaining 85 Doppler measurements, while accounting for an RV offset between the two different HARPS setups.

The RV model includes a linear and a quadratic term, to account for the long-term variation described in Sect. 5, as well as two Keplerians, to account for the Doppler reflex motion induced by HD 15337 b and HD 15337 c. The RV stellar signal at the star’s rotation period was modeled as an additional coherent sine-like curve whose period was constrained with a uniform prior centered at $P_{\text{rot}} = 36.5$ days and having a width of 0.2 days, as derived from the FWHM of the peak detected in the periodogram of the HARPS FWHMs. For the phase and amplitude of the activity signal we adopted uniform priors. While this simple model might not fully reproduce the periodic and quasi-periodic variations induced by evolving active regions carried around by stellar rotation, it has proven to be effective in accounting for the stellar signal of active and moderately active stars (e.g., Pepe et al. 2013; Gandolfi et al. 2017; Barragán et al. 2018; Prieto-Arranz et al. 2018). Any variation not properly modeled by the coherent sine-curve, and/or any instrumental noises not included in the nominal RV uncertainties, were accounted for by fitting two RV jitter terms for the two HARPS setups.

We modeled the *TESS* transit light curves using the limb-darkened quadratic model of Mandel & Agol (2002). For the limb darkening coefficients, we set Gaussian priors using the values derived by Claret (2017) for the *TESS* pass-band. We imposed conservative error bars of 0.1 on both the linear and the quadratic limb-darkening term. For the eccentricity and argument of periastron we adopted the parametrization proposed by Anderson et al. (2011). A preliminary analysis showed that the transit light curve poorly constrains the scaled semi-major axis (a/R_*). We therefore set a Gaussian prior on a/R_* using Kepler’s third law, the orbital period, and the derived stellar mass and radius (Sect. 4.2).

We imposed uniform priors for the remaining fitted parameters. Details of the fitted parameters and prior ranges are given in Table 2. We used 500 independent Markov chains initialized randomly inside the prior ranges. Once all chains converged, we used the last 5000 iterations and saved the chain states every ten iterations. This approach generates a posterior distribution of 250 000 points for each fitted parameter. Table 2 lists the inferred planetary parameters. They are defined as the median and 68% region of the credible interval of the posterior distributions for each fitted parameter. The transit and RV curves are shown in Fig. 6.

We also experimented with Gaussian Processes (GPs) to model the correlated RV noise associated with stellar activity. Gaussian Processes model stochastic processes with a parametric description of the covariance matrix. GP regression has proven to be successful in modeling the effect of stellar activity for several other exoplanetary systems (see, e.g., Haywood et al. 2014; Grunblatt et al. 2015; López-Morales et al. 2016; Barragán et al. 2018). To this aim, we modified the code `pyaneti` in order to include a GP algorithm coupled to the MCMC method. We implemented the GP approach proposed by Rajpaul et al. (2015). Briefly, this framework assumes that the star-induced RV variations and activity indicators can be modeled by the same underlying GP and its derivative. This allows the GP to disentangle the RV activity component from the planetary signals.

We assumed that the stellar activity can be modeled by the quasi-periodic kernel described by Rajpaul et al. (2015). We modeled together the HARPS RV, BIS, and FWHM time-series and we treated RV and BIS as being described by the GP and its first derivative, while for FWHM we assumed that it is only described by the GP. The fitted hyper-parameters are then V_c , V_r , B_c , B_r , L_c , as defined by Rajpaul et al. (2015), to account for the GP amplitudes of the RV, BIS, and FWHM signals, the period of the activity signal P_{GP} , the inverse of the harmonic complexity λ_p , and the long term evolution timescale λ_e . We coupled this GP approach with the joint modeling described in the previous section (omitting the extra coherent signal).

As for the planetary signals, we imposed the same priors described in the previous subsection. For the hyper-parameters, we used uniform priors, except for P_{GP} , for which we imposed a Gaussian prior with mean 36.5 d and standard deviation of 0.2 d. We used 250 chains to explore the parameters space. We created the posterior distributions with 500 iterations of converged chains, this generated a posterior distribution with 250,000 points for each parameters.

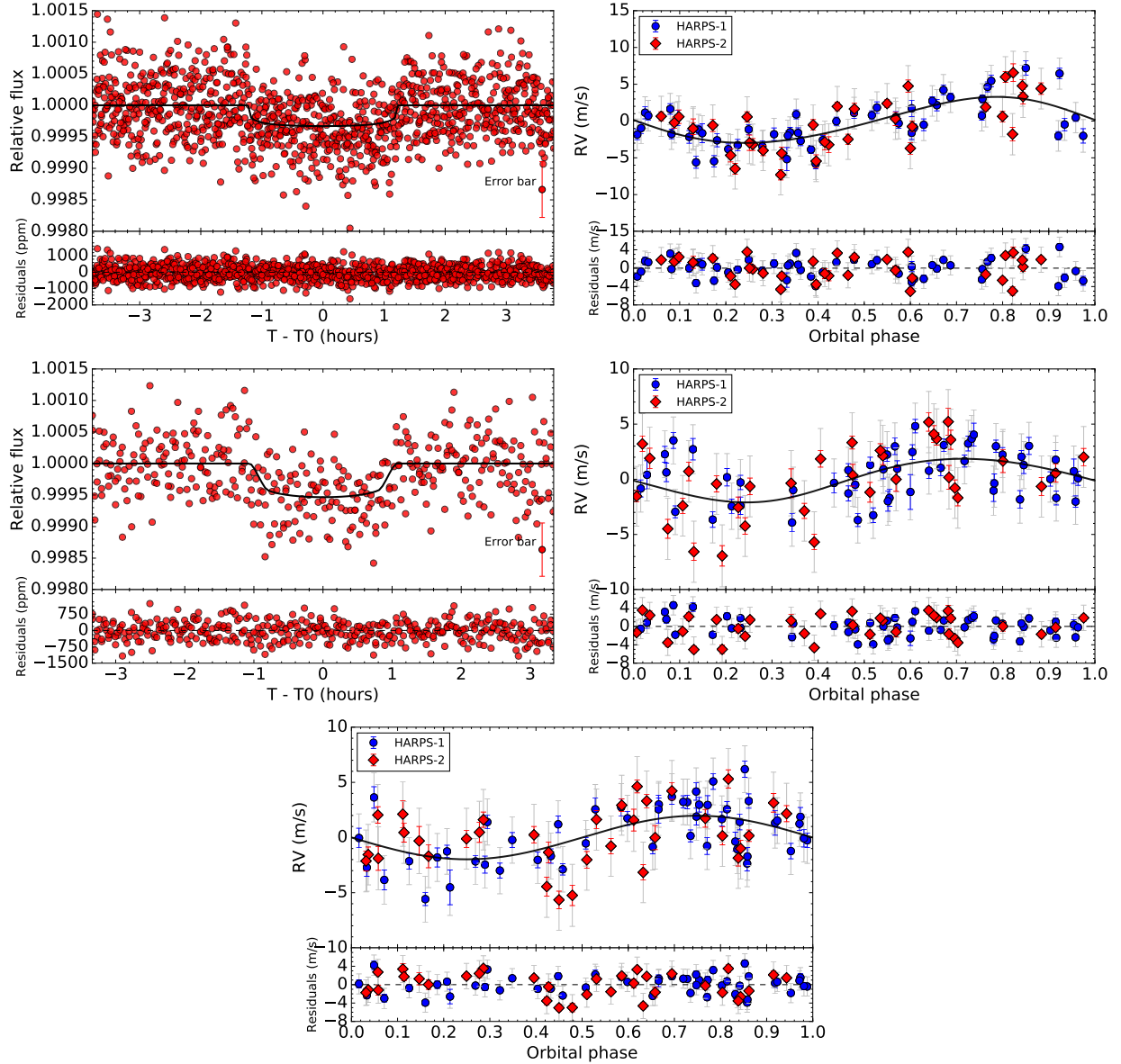


Figure 6. *Left panel.* Phase-folded transit light curves and RV curves of HD 15337 b (upper panels) and HD 15337 c (middle panels). The stellar RV signal is shown in the lower panel. The best fitting transit (left panels), Keplerian (right panels), and sine (lower panel) models are overplotted with thick black lines. The *TESS* data points are shown with red circles (left panels). The HARPS RV measurements (right panels and lower panel) are plotted with blue circles (old fiber) and red diamonds (new fiber), along with their nominal uncertainties. The vertical gray lines mark the error bars including the RV jitter. The RV curves are phase-folded to the orbital period of the two planets (right panels), and to the rotational period of the star (lower panel), following the subtraction of the systemic velocities and other signals.

For planets b and c we derived an RV semi-amplitude of $2.71^{+0.54}_{-0.51} \text{ m s}^{-1}$ and $2.06^{+0.64}_{-0.58} \text{ m s}^{-1}$, respectively, which are in very good agreement with the values reported in Table 2. The other planetary and orbital parameters are also consistent with the values presented in Table 2. For the GP hyper-parameters, we found $V_c = 0.55 \pm 0.23 \text{ m s}^{-1}$, $V_r = 70^{+27}_{-21} \text{ m s}^{-1}$, $B_c = 9.4^{+3.4}_{-2.9} \text{ m s}^{-1}$, $B_r = 64^{+20}_{-25} \text{ m s}^{-1}$, $L_c = 5.4 \pm 2.2 \text{ m s}^{-1}$, $P_{\text{GP}} = 36.5 \pm 0.2 \text{ d}$, $\lambda_e = 4217^{+624}_{-685} \text{ d}$, and $\lambda_p = 1086^{+501}_{-394}$.

The relatively large values of the scale parameters in the GP, i.e. λ_e and λ_p , indicate that the stellar activity behaves like a sinusoidal signal (with slight corrections).

7. DISCUSSION AND CONCLUSIONS

The inner-most transiting planet HD 15337 b ($P_{\text{orb},b} = 4.8 \text{ days}$) has a mass of $M_b = 7.63 \pm 0.94 M_{\oplus}$ and a radius of $R_b = 1.585 \pm 0.056 R_{\oplus}$, yielding a mean density of $\rho_b = 10.5^{+1.8}_{-1.6} \text{ g cm}^{-3}$. Figure 7 displays the position

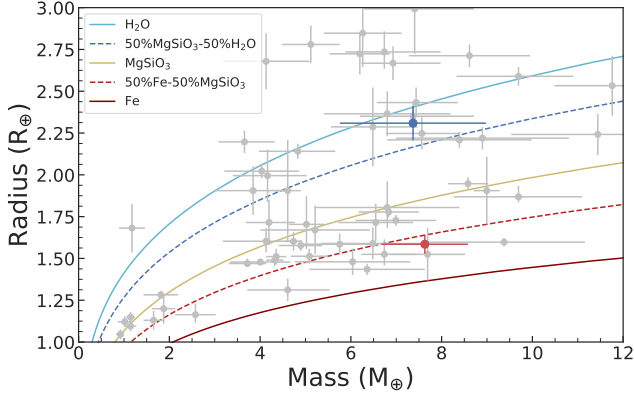


Figure 7. Mass-radius diagram for low-mass ($M_p < 12 M_\oplus$), small ($R_p < 3 R_\oplus$) planets with mass-radius measurements better than 25% (from <http://www.astro.keele.ac.uk/jkt/tepcat/>; Southworth 2011). Composition models from Zeng et al. (2016) are displayed with different lines and colors. The solid red and blue circles mark the position of HD 15337 b and HD 15337 c, respectively.

of HD 15337 b on the mass-radius diagram compared to the sub-sample of small transiting planets ($R \leq 4 R_\oplus$) whose masses and radii have been derived with a precision better than 25%. Theoretical models from Zeng et al. (2016) are overplotted using different lines and colors. Given the precision of our mass determination ($\sim 13\%$), we conclude that HD 15337 b is a rocky terrestrial planet with a composition consisting of $\sim 50\%$ silicate and $\sim 50\%$ iron.

For HD 15337, we obtained a mass of $M_c = 7.37^{+1.63}_{-1.61} M_\oplus$ and a radius of $R_c = 2.309^{+0.110}_{-0.103} R_\oplus$, yielding a mean density of $\rho_c = 3.3^{+0.9}_{-0.8} \text{ g cm}^{-3}$. Therefore, HD 15337 b and c have virtually the same mass, but the radius of HD 15337 c is ~ 1.5 larger than the radius of HD 15337 b. The lower bulk density of HD 15337 c suggests that the planet is likely composed by a rocky core surrounded either by a considerable amount of water, or by a light, hydrogen-dominated envelope. In the first case, the amount of water and high planetary equilibrium temperature would imply the presence of a steam atmosphere, which would be strongly hydrogen dominated in its upper part as a consequence of water dissociation and of the low mass of hydrogen. It is therefore plausible to assume that HD 15337 c hosts a hydrogen-dominated atmosphere, at least in its upper part.

As in other systems hosting two close-in sub-Neptune-mass planets (e.g., HD 3167 Gandolfi et al. 2017), the radii of HD 15337 b and c lie on opposite sides of the radius gap (Fulton et al. 2017; Van Eylen et al. 2018), with the closer-in planet having a higher bulk density, similarly to what observed in other close-in systems with measured planetary masses (e.g., K2-109,

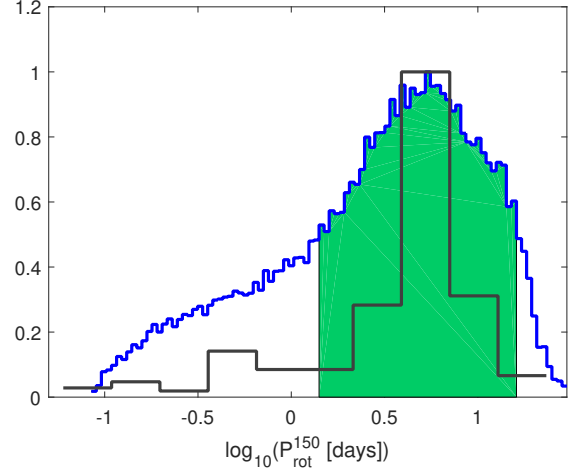


Figure 8. MCMC posterior distributions for the stellar rotation period at an age of 150 Myr obtained from the modeling of HD 15337 c. The shaded areas correspond to the 68% highest posterior density credible interval. The black histogram shows the distribution of stellar rotation periods measured for open cluster stars with an age of 150 Myr (from Johnstone et al. 2015).

HD 3167, GJ 9827 Guenther et al. 2017; Gandolfi et al. 2017; Prieto-Arranz et al. 2018). This gap is believed to be caused by atmospheric escape (Owen & Wu 2017; Jin & Mordasini 2018), which is stronger for closer-in planets. Within this context, HD 15337 b has probably lost its primary, hydrogen-dominated atmosphere, and now hosts a secondary atmosphere possibly resulting from out-gassing of a solidifying magma ocean, while HD 15337 c is likely to still partly retain the primordial hydrogen-dominated envelope. This is consistent with Van Eylen et al. (2018), who measured the location and slope of the radius gap as a function of orbital period and matched it to models suggesting a homogeneous terrestrial core composition.

The present-day properties of the atmospheres of HD 15337 b and c are therefore intimately related to the amount of high-energy (X-ray and EUV; $< 91.2 \text{ nm}$) stellar radiation received since the dispersal of the protoplanetary nebula, and thus also to the stellar rotation history. The evolution of the stellar rotation rate does not follow a unique path because stars of the same mass and metallicity can have significantly different rotation rates up to about 1 Gyr (e.g., Mamajek & Hillenbrand 2008; Johnstone et al. 2015; Tu et al. 2015). For older stars, it is therefore not possible to infer their past high-energy emission from their measured stellar properties. Starting from the assumption that HD 15337 c hosts a hydrogen-dominated atmosphere, we derive the history of the stellar rotation and high-energy emission by mod-

eling the atmospheric evolution of HD 15337 c. To this end, we employ the atmospheric evolution algorithm described by Kubyshkina et al. (2018) and further developed by Kubyshkina et al. (2019, submitted), which is based on a Bayesian approach fitting the currently observed planetary radius, combining the planetary evolution model with the open-source MCMC algorithm of Cubillos et al. (2017). The planetary atmospheric evolution model, system parameters (i.e., planetary mass, planetary radius, orbital separation, current stellar rotation period, stellar age, stellar mass) are then used to compute the posterior distribution for the stellar rotation rate at any given age via MCMC. We assumed Gaussian priors determined by the measured system parameters and their uncertainties.

Figure 8 shows the obtained posterior distribution for the rotation period HD 15337 at an age of 150 Myr in comparison with the distribution derived from measurements of open cluster stars of the same age (Johnstone et al. 2015). Our results indicate that HD 15337, when it was young, was likely to be a moderate rotator, with a high-energy emission at 150 Myr ranging between 1.5 and 93 times the current solar emission, further excluding that the star was a very fast/slow rotator.

The position of HD 15337 c in the mass-radius diagram (Fig. 7) indicates that the planet may be hosting a massive hydrogen-dominated envelope or a smaller secondary atmosphere. As primary atmospheres are easily subject to escape, knowing the current composition of the envelope of HD 15337 c would provide a strong constrain on atmospheric evolution models. In this respect, this planet is similar to π Men c (Gandolfi et al. 2018; Huang et al. 2018); furthermore, as for π Men, the close distance to the system and brightness of the host star would enable high-quality transmission spectroscopy observations spanning from far-ultraviolet to infrared wavelengths. Of particular interest would be far-ultraviolet observations covering H I, C II, and O I resonance lines, that could be obtained with the *Hubble Space Telescope* and would ideally probe the nature of the atmosphere, thus constraining atmospheric escape and evolution models.

We acknowledge the use of public *TESS* Alert data from pipelines at the *TESS* Science Office and at the

TESS Science Processing Operations Center. This paper includes data collected by the *TESS* mission, which are publicly available from the Mikulski Archive for Space Telescopes (MAST). Funding for the *TESS* mission is provided by NASA’s Science Mission directorate. Based on observations collected at the European Organization for Astronomical Research in the Southern Hemisphere under ESO programs 072.C-0488, 183.C-0972, 192.C-0852, 196.C-1006, and 198.C-0836. This research has made use of the services of the ESO Science Archive Facility. LF and DK acknowledge the Austrian Forschungsförderungsgesellschaft FFG project “TAPAS4CHEOPS” P853993. JHL acknowledges the support of the Japan Society for the Promotion of Science (JSPS) Research Fellowship for Young Scientists. JK, SG, MP, SC, KWFL, HR, AH and ME acknowledge the support by DFG Grants PA525/18-1, PA525/19-1, PA-525/20-1, HA 3279/12-1 and RA 714/14-1 within the DFG Priority Program SPP1992: ‘Exploring the Diversity of Exoplanets’. HJD and DN acknowledge support by grants ESP2015-65712-C5-4-R and ESP2017-87676-C5-4-R of the Spanish Secretary of State for R&D&i (MINECO). SC thanks the Hungarian National Research, Development and Innovation Office for the NKFI-KH-130372 grant. IR acknowledges support from the Spanish Ministry for Science, Innovation and Universities (MCIU) and the Fondo Europeo de Desarrollo Regional (FEDER) through grant ESP2016-80435-C2-1-R, as well as the support of the Generalitat de Catalunya/CERCA programme. MF and CMP gratefully acknowledge the support of the Swedish National Space Agency. 17-01752J. MS acknowledges the Postdoc@MUNI project CZ.02.2.69/0.0/0.0/16-027/0008360.

Facilities: *TESS*, HARPS

Software: VARLET (Grziwa & Pätzold 2016), PHALET (Grziwa & Pätzold 2016), SME (Valenti & Piskunov 1996; Valenti & Fischer 2005; Piskunov & Valenti 2017), *exotrending* (Barragán & Gandolfi 2017), *pyaneti* (Barragán et al. 2019)

REFERENCES

- Alibert, Y., & Benz, W. 2017, *A&A*, 598, L5
- Alibert, Y., Mousis, O., Mordasini, C., & Benz, W. 2005, *ApJL*, 626, L57
- Anderson, D. R., Collier Cameron, A., Hellier, C., et al. 2011, *ApJL*, 726, L19
- Axer, M., Fuhrmann, K., & Gehren, T. 1994, *A&A*, 291, 895

Table 2. HD 15337 system parameters.

Parameter	Prior ^(a)	Derived value
Stellar parameters		
Star mass M_* (M_\odot)	...	0.90 ± 0.03
Star radius R_* (R_\odot)	...	0.856 ± 0.017
Effective Temperature T_{eff} (K)	...	5125 ± 50
Surface gravity ^(b) $\log g_*$ (cgs)	...	4.52 ± 0.02
Surface gravity ^(c) $\log g_*$ (cgs)	...	4.40 ± 0.10
Iron abundance [Fe/H] (dex)	...	0.15 ± 0.10
Projected rotational velocity $v \sin i_*$ (km s^{-1})	...	1.0 ± 1.0
Age (Gyr)	...	5.1 ± 0.8
Interstellar extinction A_v	...	0.02 ± 0.02
Model parameters of HD 15337 b		
Orbital period $P_{\text{orb, b}}$ (days)	$\mathcal{U}[4.73, 4.78]$	4.756216 ± 0.000081
Transit epoch $T_{0, \text{b}}$ (BJD _{TDB} - 2 450 000)	$\mathcal{U}[8411.35, 8411.55]$	8411.46165 ± 0.00057
Scaled semi-major axis a_b/R_*	$\mathcal{N}[13.11, 0.17]$	13.44 ± 0.30
Planet-to-star radius ratio R_b/R_*	$\mathcal{U}[0, 0.1]$	0.01698 ± 0.00050
Impact parameter b_b	$\mathcal{U}[0, 1]$	$0.30^{+0.15}_{-0.19}$
$\sqrt{e_b} \sin \omega_{*, \text{b}}$	$\mathcal{U}[-1, 1]$	$0.13^{+0.12}_{-0.19}$
$\sqrt{e_b} \cos \omega_{*, \text{b}}$	$\mathcal{U}[-1, 1]$	$0.20^{+0.14}_{-0.21}$
Radial velocity semi-amplitude variation K_b (m s^{-1})	$\mathcal{U}[0, 10]$	3.13 ± 0.39
Model parameters of HD 15337 c		
Orbital period $P_{\text{orb, c}}$ (days)	$\mathcal{U}[17.08, 17.28]$	17.17753 ± 0.00077
Transit epoch $T_{0, \text{c}}$ (BJD _{TDB} - 2 450 000)	$\mathcal{U}[8414.4, 8414.7]$	$8414.55162^{+0.00076}_{-0.00073}$
Scaled semi-major axis a_c/R_*	$\mathcal{N}[13.11, 0.17]$	31.68 ± 0.73
Planet-to-star radius ratio R_c/R_*	$\mathcal{U}[0, 0.1]$	0.0247 ± 0.0010
Impact parameter b_c	$\mathcal{U}[0, 1]$	0.88 ± 0.03
$\sqrt{e_c} \sin \omega_{*, \text{c}}$	$\mathcal{U}[-1, 1]$	$-0.07^{+0.29}_{-0.27}$
$\sqrt{e_c} \cos \omega_{*, \text{c}}$	$\mathcal{U}[-1, 1]$	$-0.02^{+0.17}_{-0.18}$
Radial velocity semi-amplitude variation K_c (m s^{-1})	$\mathcal{U}[0, 10]$	1.98 ± 0.43
Additional model parameters		
Parameterized limb-darkening coefficient q_1	$\mathcal{N}[0.43, 0.1]$	0.37 ± 0.10
Parameterized limb-darkening coefficient q_2	$\mathcal{N}[0.19, 0.1]$	0.18 ± 0.10
Systemic velocity γ_{HS1} (km s^{-1})	$\mathcal{U}[-4.0, -3.6]$	-3.8172 ± 0.0024
Systemic velocity γ_{HS2} (km s^{-1})	$\mathcal{U}[-4.0, -3.6]$	-3.7976 ± 0.0011
RV jitter term σ_{HS1} (m s^{-1})	$\mathcal{U}[0, 100]$	$1.99^{+0.27}_{-0.24}$
RV jitter term σ_{HS2} (m s^{-1})	$\mathcal{U}[0, 100]$	$2.65^{+0.43}_{-0.37}$
Stellar rotation period (P_{rot}) days	$\mathcal{U}[36.4, 36.6]$	36.539 ± 0.024
Linear RV term $\text{m s}^{-1} \text{d}^{-1}$	$\mathcal{U}[-100, 100]$	-0.0056 ± 0.0015
Quadratic RV term $\text{m s}^{-1} \text{d}^{-1}$	$\mathcal{U}[-100, 100]$	-0.0000013 ± 0.0000002
Derived parameters of HD 15337 b		
Planet mass M_b (M_\oplus)	...	7.63 ± 0.94
Planet radius R_b (R_\oplus)	...	1.585 ± 0.056
Planet mean density ρ_b (g cm^{-3})	...	$10.5^{+1.8}_{-1.6}$
Semi-major axis of the planetary orbit a_c (AU)	...	0.0535 ± 0.0016
Orbit eccentricity e_c	...	0.09 ± 0.06
Orbit inclination i_c (deg)	...	$88.7^{+0.8}_{-0.6}$
Equilibrium temperature ^(d) $T_{\text{eq, c}}$ (K)	...	989 ± 15
Transit duration $\tau_{14, \text{c}}$ (hours)	...	2.518 ± 0.036
Derived parameters of HD 15337 c		
Planet mass M_c (M_\oplus)	...	$7.37^{+1.63}_{-1.61}$
Planet radius R_c (R_\oplus)	...	$2.309^{+0.110}_{-0.103}$
Planet mean density ρ_c (g cm^{-3})	...	$3.3^{+0.9}_{-0.8}$
Semi-major axis of the planetary orbit a_c (AU)	...	0.1261 ± 0.0038
Orbit eccentricity e_c	...	$0.08^{+0.10}_{-0.06}$
Orbit inclination i_c (deg)	...	88.4 ± 0.1
Equilibrium temperature ^(d) $T_{\text{eq, c}}$ (K)	...	644 ± 10
Transit duration $\tau_{14, \text{c}}$ (hours)	...	$2.229^{+0.070}_{-0.060}$

NOTE—(a) $\mathcal{U}[a, b]$ refers to uniform priors between a and b , and $\mathcal{F}[a]$ to a fixed a value; (b) from spectroscopy and isochrones; (c) from spectroscopy; (d) assuming zero albedo and uniform redistribution of heat.

Table 3. HARPS RV measurements of HD 15337 acquired with the old fiber bundle.

BJD _{TDB} ^a -2450000	RV (km s ⁻¹)	$\pm\sigma$ (km s ⁻¹)	BIS (km s ⁻¹)	FWHM (km s ⁻¹)	T _{exp} (s)	S/N ^b
2988.663700	-3.8208	0.0010	0.0013	6.1330	900	70.8
3270.822311	-3.8260	0.0008	0.0015	6.1353	900	93.7
3785.541537	-3.8234	0.0007	0.0010	6.1471	900	101.7
4422.673842	-3.8155	0.0006	0.0059	6.1571	900	108.1
4424.646720	-3.8111	0.0007	0.0037	6.1531	900	97.7
4427.703292	-3.8185	0.0006	0.0049	6.1547	900	101.4
4428.644416	-3.8170	0.0005	0.0034	6.1481	900	125.8
4484.550086	-3.8203	0.0006	0.0063	6.1631	900	102.6
4730.822010	-3.8128	0.0006	0.0100	6.1779	900	108.1
4731.764597	-3.8127	0.0007	0.0133	6.1767	900	98.8
4734.786220	-3.8132	0.0010	0.0150	6.1661	900	68.4
4737.774983	-3.8115	0.0011	0.0053	6.1684	900	62.2
4739.782074	-3.8140	0.0008	0.0015	6.1633	1200	79.4
4801.645505	-3.8101	0.0006	0.0061	6.1753	900	112.5
4802.681221	-3.8117	0.0007	0.0065	6.1745	900	100.7
4803.585301	-3.8107	0.0006	0.0078	6.1681	900	117.0
4804.621351	-3.8088	0.0008	0.0102	6.1717	900	85.6
4806.641716	-3.8139	0.0006	0.0078	6.1734	900	103.1
4847.567925	-3.8116	0.0006	0.0062	6.1635	900	113.6
5038.928157	-3.8169	0.0006	0.0088	6.1583	900	113.4
5039.878459	-3.8165	0.0009	0.0028	6.1577	900	78.1
5040.884957	-3.8191	0.0016	-0.0011	6.1644	900	47.0
5042.901725	-3.8105	0.0005	0.0036	6.1476	900	120.8
5067.879903	-3.8164	0.0007	0.0068	6.1558	900	93.6
5068.916098	-3.8185	0.0008	0.0056	6.1655	800	85.2
5070.833766	-3.8159	0.0008	0.0071	6.1630	900	84.5
5097.828049	-3.8123	0.0008	0.0012	6.1615	900	79.2
5100.771149	-3.8063	0.0007	0.0049	6.1668	900	91.2
5106.752698	-3.8165	0.0009	0.0080	6.1621	900	76.6
5108.758136	-3.8147	0.0009	0.0105	6.1507	900	73.4
5110.725697	-3.8138	0.0007	0.0023	6.1464	900	89.9
5113.727962	-3.8110	0.0006	0.0041	6.1508	900	116.6
5116.732322	-3.8188	0.0008	0.0028	6.1553	900	85.7
5124.719074	-3.8125	0.0005	0.0052	6.1507	900	126.2
5134.807289	-3.8104	0.0007	0.0066	6.1632	900	94.7
5137.624046	-3.8095	0.0006	0.0115	6.1656	900	102.7
5141.642265	-3.8120	0.0006	0.0095	6.1629	900	111.4
5164.557710	-3.8122	0.0006	0.0038	6.1587	900	104.4
5166.557368	-3.8099	0.0006	0.0008	6.1533	900	104.2
5169.552068	-3.8161	0.0005	0.0008	6.1593	900	120.8
5227.530636	-3.8150	0.0007	0.0091	6.1510	900	98.7
5230.529883	-3.8161	0.0007	-0.0025	6.1456	900	94.4
5245.518763	-3.8120	0.0007	0.0087	6.1559	900	97.8
5246.519846	-3.8169	0.0360	0.1136	6.3367	5	3.8
5246.526257	-3.8094	0.0007	0.0047	6.1576	900	94.9
6620.642369	-3.8098	0.0007	-0.0005	6.1539	1200	92.8
6623.580646	-3.8089	0.0010	0.0033	6.1612	900	69.8
6625.634172	-3.8073	0.0008	0.0024	6.1609	900	92.2
6628.589169	-3.8119	0.0013	0.0010	6.1674	900	58.4
6631.568567	-3.8060	0.0008	0.0040	6.1663	900	90.9
7036.603445	-3.8091	0.0009	0.0001	6.1772	900	83.9
7037.560130	-3.8147	0.0008	0.0041	6.1679	900	88.9

NOTE—(a) Barycentric Julian dates are given in barycentric dynamical time; (b) S/N per pixel at 550 nm; (*) outlier not included in the analysis.

Table 4. HARPS RV measurements of HD 15337 acquired with the new fiber bundle.

BJD _{TDB} ^a -2450000	RV (km s ⁻¹)	$\pm\sigma$ (km s ⁻¹)	BIS (km s ⁻¹)	FWHM (km s ⁻¹)	T _{exp} (s)	S/N ^b
7291.826359	-3.7848	0.0008	0.0273	6.2102	900	88.1
7292.799439	-3.7889	0.0007	0.0246	6.2141	900	95.6
7299.843584	-3.7988	0.0007	0.0229	6.1968	900	106.2
7303.879389	-3.7973	0.0013	0.0184	6.1985	900	60.3
7353.698805	-3.7959	0.0008	0.0209	6.2081	900	97.6
7357.682828	-3.7898	0.0006	0.0239	6.2073	900	127.1
7373.685080	-3.7889	0.0007	0.0207	6.2064	900	99.5
7395.644348	-3.7931	0.0011	0.0253	6.2093	900	68.5
7399.617257	-3.7938	0.0008	0.0213	6.1981	900	90.1
7418.584180	-3.7951	0.0007	0.0267	6.1927	900	108.5
7422.589672	-3.7969	0.0008	0.0211	6.1964	900	103.2
7427.538475	-3.7932	0.0008	0.0197	6.1990	900	94.5
7429.539077	-3.7883	0.0006	0.0222	6.2054	900	129.3
7584.927622	-3.7969	0.0007	0.0218	6.2010	900	97.2
7613.935104	-3.8009	0.0007	0.0214	6.1960	900	104.8
7641.794439	-1.6179	0.0009	0.0220	6.1919	900	81.4
7642.837840	-3.8015	0.0009	0.0196	6.1934	900	80.2
7643.808690	-3.8000	0.0008	0.0189	6.1928	900	89.1
7644.862657	-3.7982	0.0009	0.0202	6.1907	900	79.1
7647.923051	-3.7972	0.0007	0.0181	6.1888	900	110.7
7649.726575	-3.7895	0.0010	0.0205	6.1981	900	72.2
7650.752860	-3.7912	0.0006	0.0207	6.2017	900	115.2
7652.744706	-3.7889	0.0008	0.0222	6.1982	900	91.5
7656.751475	-3.7956	0.0008	0.0254	6.2022	900	87.1
7658.854305	-3.7910	0.0005	0.0196	6.1970	900	142.1
7660.797461	-3.7952	0.0008	0.0195	6.1985	900	85.9
7661.831637	-3.7959	0.0007	0.0116	6.2990	900	107.0
7971.834240	-3.7981	0.0009	0.0219	6.1895	900	79.6
7993.916286	-3.8000	0.0009	0.0246	6.2071	900	84.7
7994.887034	-3.7979	0.0011	0.0250	6.2032	900	70.0
7996.829372	-3.7884	0.0012	0.0185	6.2004	900	64.2
7996.923718	-3.7902	0.0009	0.0238	6.1989	1500	89.6
7998.866747	-3.7986	0.0010	0.0216	6.2004	900	72.2
8001.872927	-3.7930	0.0008	0.0188	6.1873	900	99.5
8002.895001	-3.7975	0.0009	0.0216	6.1880	900	82.8

NOTE—(a) Barycentric Julian dates are given in barycentric dynamical time; (b) S/N per pixel at 550 nm; (*) outlier not included in the analysis.

- Baranne, A., Queloz, D., Mayor, M., et al. 1996, *A&AS*, 119, 373
- Barragán, O., & Gandolfi, D. 2017, Exotrending: Fast and easy-to-use light curve detrending software for exoplanets, *Astrophysics Source Code Library*, , , ascl:1706.001
- Barragán, O., Gandolfi, D., & Antoniciello, G. 2019, *MNRAS*, 482, 1017
- Barragán, O., Gandolfi, D., Dai, F., et al. 2018, *A&A*, 612, A95
- Bruntt, H., Bedding, T. R., Quirion, P.-O., et al. 2010, *MNRAS*, 405, 1907
- Christiansen, J. L., Jenkins, J. M., Caldwell, D. A., et al. 2012, *PASP*, 124, 1279
- Claret, A. 2017, *A&A*, 600, A30
- Cubillos, P., Harrington, J., Lored, T. J., et al. 2017, *AJ*, 153, 3
- Cutri, R. M., & et al. 2013, *VizieR Online Data Catalog*, 2328
- Cutri, R. M., Skrutskie, M. F., van Dyk, S., et al. 2003, 2MASS All Sky Catalog of point sources.
- Doyle, A. P., Davies, G. R., Smalley, B., Chaplin, W. J., & Elsworth, Y. 2014, *MNRAS*, 444, 3592
- Esposito, M., Armstrong, D. J., Gandolfi, D., et al. 2018, arXiv e-prints, arXiv:1812.05881
- Fuhrmann, K., Axer, M., & Gehren, T. 1993, *A&A*, 271, 451
- . 1994, *A&A*, 285, 585
- Fuhrmann, K., Pfeiffer, M., Frank, C., Reetz, J., & Gehren, T. 1997a, *A&A*, 323, 909
- Fuhrmann, K., Pfeiffer, M. J., & Bernkopf, J. 1997b, *A&A*, 326, 1081
- Fulton, B. J., Petigura, E. A., Howard, A. W., et al. 2017, *AJ*, 154, 109
- Gaia Collaboration, Brown, A. G. A., Vallenari, A., et al. 2018, *A&A*, 616, A1
- Gandolfi, D., Barragán, O., Hatzes, A. P., et al. 2017, *AJ*, 154, 123
- Gandolfi, D., Barragán, O., Livingston, J. H., et al. 2018, *A&A*, 619, L10
- Gomes da Silva, J., Santos, N. C., Boisse, I., Dumusque, X., & Lovis, C. 2014, *A&A*, 566, A66
- Grunblatt, S. K., Howard, A. W., & Haywood, R. D. 2015, *ApJ*, 808, 127
- Grziwa, S., & Pätzold, M. 2016, ArXiv e-prints, arXiv:1607.08417
- Guenther, E. W., Barragan, O., Dai, F., et al. 2017, ArXiv e-prints, arXiv:1705.04163
- Haywood, R. D., Collier Cameron, A., Queloz, D., et al. 2014, *MNRAS*, 443, 2517
- Høg, E., Fabricius, C., Makarov, V. V., et al. 2000, *A&A*, 355, L27
- Huang, C. X., Burt, J., Vanderburg, A., et al. 2018, *ApJL*, 868, L39
- Jenkins, J. M., Twicken, J. D., McCauliff, S., et al. 2016, in *Proc. SPIE*, Vol. 9913, Software and Cyberinfrastructure for Astronomy IV, 99133E
- Jin, S., & Mordasini, C. 2018, *ApJ*, 853, 163
- Johnstone, C. P., Güdel, M., Brott, I., & Lüftinger, T. 2015, *A&A*, 577, A28
- Jones, M. I., Brahm, R., Espinoza, N., et al. 2018, arXiv e-prints, arXiv:1811.05518
- Kovács, G., Zucker, S., & Mazeh, T. 2002, *A&A*, 391, 369
- Kubyskhina, D., Fossati, L., Erkaev, N. V., et al. 2018, *A&A*, 619, A151
- Kuerster, M., Schmitt, J. H. M. M., Cutispoto, G., & Dennerl, K. 1997, *A&A*, 320, 831
- Kurucz, R. L. 2013, ATLAS12: Opacity sampling model atmosphere program, *Astrophysics Source Code Library*, , , ascl:1303.024
- Lo Curto, G., Pepe, F., Avila, G., et al. 2015, *The Messenger*, 162, 9
- López-Morales, M., Haywood, R. D., Coughlin, J. L., et al. 2016, *AJ*, 152, 204
- Mamajek, E. E., & Hillenbrand, L. A. 2008, *ApJ*, 687, 1264
- Mandel, K., & Agol, E. 2002, *ApJL*, 580, L171
- Mayor, M., Pepe, F., Queloz, D., et al. 2003, *The Messenger*, 114, 20
- Nielsen, L. D., Bouchy, F., Turner, O., et al. 2018, arXiv e-prints, arXiv:1811.01882
- Owen, J. E., & Wu, Y. 2017, *ApJ*, 847, 29
- Paunzen, E. 2015, *A&A*, 580, A23
- Pepe, F., Cameron, A. C., Latham, D. W., et al. 2013, *Nature*, 503, 377
- Piskunov, N., & Valenti, J. A. 2017, *A&A*, 597, A16
- Prieto-Arranz, J., Palle, E., Gandolfi, D., et al. 2018, *A&A*, 618, A116
- Quinn, S. N., Becker, J. C., Rodriguez, J. E., et al. 2019, arXiv e-prints, arXiv:1901.09092
- Rajpaul, V., Aigrain, S., Osborne, M. A., Reece, S., & Roberts, S. 2015, *MNRAS*, 452, 2269
- Ricker, G. R., Winn, J. N., Vanderspek, R., et al. 2015, *Journal of Astronomical Telescopes, Instruments, and Systems*, 1, 014003
- Schlegel, D. J., Finkbeiner, D. P., & Davis, M. 1998, *ApJ*, 500, 525
- Smith, J. C., Stumpe, M. C., Van Cleve, J. E., et al. 2012, *Publications of the Astronomical Society of the Pacific*, 124, 1000
- Southworth, J. 2011, *MNRAS*, 417, 2166

- Spada, F., Demarque, P., Kim, Y.-C., & Sills, A. 2013, *ApJ*, 776, 87
- Stassun, K. G., Collins, K. A., & Gaudi, B. S. 2017, *AJ*, 153, 136
- Stassun, K. G., Corsaro, E., Pepper, J. A., & Gaudi, B. S. 2018a, *AJ*, 155, 22
- Stassun, K. G., & Torres, G. 2016, *AJ*, 152, 180
- . 2018, *ApJ*, 862, 61
- Stassun, K. G., Oelkers, R. J., Pepper, J., et al. 2018b, *AJ*, 156, 102
- Stumpe, M. C., Smith, J. C., Van Cleve, J. E., et al. 2012, *Publications of the Astronomical Society of the Pacific*, 124, 985
- Torres, G., Andersen, J., & Giménez, A. 2010, *A&A Rv*, 18, 67
- Trifonov, T., Stock, S., Henning, T., et al. 2019, *AJ*, 157, 93
- Tu, L., Johnstone, C. P., Güdel, M., & Lammer, H. 2015, *A&A*, 577, L3
- Valenti, J. A., & Fischer, D. A. 2005, *ApJS*, 159, 141
- Valenti, J. A., & Piskunov, N. 1996, *A&AS*, 118, 595
- Van Eylen, V., Agentoft, C., Lundkvist, M. S., et al. 2018, *MNRAS*, 479, 4786
- Yi, S., Demarque, P., Kim, Y.-C., et al. 2001, *ApJS*, 136, 417
- Zechmeister, M., & Kürster, M. 2009, *A&A*, 496, 577
- Zeng, L., Sasselov, D. D., & Jacobsen, S. B. 2016, *ApJ*, 819, 127